Comparative Study of Numerical Analysis and Wind Tunnel Experiments on the Flight Behavior of a Quadcopter Drone under Disturbance Winds

Kaisei Nomura[1[0009-0008-4915-8403]], Ayato Takii[2[0000−0003−3257−7640]], Masashi Yamakawa[1,3,4[0000−0001−5960−2602]], Yusei Kobayashi[1,4[0000−0002−5690−2033]], Takahiro Ikeda[3,4[0009−0008−7496−9056]], Shinichi Asao[5[0000−0003−4326−8480]] and Seiichi Takeuchi[5]

[1] Kyoto Institute of Technology, Matsugasaki, Sakyo-ku, Kyoto 606-8585, Japan
kaikai6262nom.you@gmail.com
[2] Kobe University, 1-1, Rokkodai-cho, Nada-ku, Kobe, 657-8501, Hyogo, Japan
[3] Center for the Possible Futures, Kyoto Institute of Technology, Matsugasaki, Sakyo-ku 606-8585, Kyoto, Japan
[4] High-Performance Simulation Research Center, Kyoto Institute of Technology, Matsugasaki, Sakyo-ku 606-8585, Kyoto, Japan
[5] College of Industrial Technology, 1-27-1, Amagasaki, Hyogo 661-0047, Japan

Abstract. This study presents a computationally efficient framework for early-stage design evaluation of next-generation air mobility systems. A coupled fluid–rigid body motion analysis combining the Moving Computational Domain (MCD) method with a multi-axis sliding mesh technique was quantitatively validated against wind tunnel experiments of a quadcopter subjected to frontal disturbance winds. An inviscid fluid formulation was employed while preserving dynamic motion coupling. The results demonstrate that the predicted pitch angle under disturbance winds (0-5 m/s) agreed with experimental measurements within a maximum error of 1.56°, accurately reproducing the aircraft's dynamic equilibrium response. Rotor rotational speeds were predicted with an average relative error of approximately 10 %, and their variation with wind velocity exhibited strong correlation with experimental trends. These findings confirm that the proposed framework provides practical predictive capability with significantly reduced computational cost, making it suitable for rapid behavior assessment during early design stages. The present study represents a step toward the realization of a scalable physics-based digital twin for multirotor aircraft. Future work will focus on improving rotor thrust prediction accuracy through refined geometric modeling.

Keywords: CFD, Quadcopter Drone, Flying Car, Validation

1 Introduction

In recent years, the development of flying cars (eVTOLs) and unmanned aerial vehicles (UAVs) equipped with multiple rotors has accelerated worldwide as next-generation air mobility solutions aimed at addressing serious societal challenges such as urban

ICCS Camera Ready Version 2026
To cite this paper please use the final published version:
DOI: 10.1007/978-3-032-29924-6_2

traffic congestion and aging infrastructure [1]. These vehicles are anticipated as new transportation systems utilizing near-ground airspace that has not traditionally been used by conventional aircraft. However, because they operate at low altitudes in close proximity to people, they require an extremely high level of safety exceeding that of existing aircraft. The development of new airframe designs and control systems entails enormous costs and time. Consequently, computational fluid dynamics (CFD) simulations are expected to play a crucial role in reducing risks and improving efficiency during the early stages of the development cycle.

Research on the aerodynamic characteristics of multirotor aircraft has progressed through multifaceted approaches. Previous studies have covered a wide range of topics, from evaluating the characteristics of individual rotors [2, 3] to investigating ground effects [4] and the influence of interference flows on vehicle stability [5]. In this context, our research group proposed the concept of a "digital flying car" [6] and has conducted studies aimed at reproducing high-fidelity flight phenomena in a virtual environment. Specifically, we have investigated the effects of takeoff downwash on the ground [7], turning maneuvers [8], and aircraft behavior during propeller failure emergencies [9], based on assumed flight dynamics of a flying car. Furthermore, to address wind disturbances encountered in real-world operations, forward and turning flight simulations under strong wind conditions were performed [10], demonstrating the impact of wind on aircraft behavior.

However, these studies have primarily focused on comparisons within numerical simulations and on understanding the behavior of idealized models. Direct validation of the numerical methods through comparison with detailed experimental data obtained from actual aircraft has not yet been conducted. In particular, small quadcopters have relatively low inertia compared to large aircraft and are therefore highly susceptible to external wind disturbances [11]. Clarifying the mechanisms of attitude recovery and control response to such disturbances in small aircraft provides a fundamental basis for safety assessments when scaling up to flying cars in the future, as both share the common flight principle of multi-rotor configurations. Therefore, reproducing realistic flight conditions within the computational domain without constraining the airframe and elucidating the overall system behavior remains a critical challenge in next-generation mobility development.

Accordingly, this study performed numerical flight simulations using an inviscid fluid model. Although inviscid calculations have been reported to show good agreement with experimental data within a certain high angle-of-attack range during early-stage aerodynamic evaluations of aircraft [12], the validity of the inviscid approximation under dynamic flight conditions of multirotor aircraft, which are characterized by complex rotor–rotor interactions and abrupt attitude changes, requires further verification. To address this complex moving boundary problem, a numerical framework combining the Moving Computational Domain (MCD) method [13], based on an unstructured moving-grid finite volume method [14], with a multi-axis sliding mesh method [15] was adopted. The MCD method strictly satisfies geometric conservation laws while avoiding grid failure associated with large aircraft attitude changes, making it suitable for describing large-amplitude motions. Furthermore, the simulations were performed in a parallel computing environment using unstructured grids [16]. The originality of

ICCS Camera Ready Version 2026
To cite this paper please use the final published version:
DOI: 10.1007/978-3-032-29924-6_2

this study lies in the first quantitative validation of the proposed analytical method. This was accomplished by comparing the dynamic response of the entire system, in which the aircraft autonomously adjusts its attitude to reach an equilibrium state under external wind disturbances, with wind tunnel experimental results obtained using an actual aircraft, while inheriting the analytical framework established in previous studies. For validation, an experimental aircraft installed in a wind tunnel was used to precisely measure the propeller rotational speeds and aircraft attitude angles while maintaining hover against frontal disturbance winds. In the simulations, identical external wind speed conditions were imposed. By comparing the numerical predictions of the aircraft response with the experimental data, the prediction accuracy of the method and the associated sources of error were evaluated. This approach represents a pioneering step toward establishing a practical digital twin capable of reproducing the dynamic behavior of real aircraft in a virtual environment, thereby contributing to reduced design time and enhanced reliability.

2 Experimental Overview

2.1 Test Aircraft

The experiments were conducted using ACSL's small aerial photography drone "SOTEN" [17]. The main specifications of the aircraft are summarized in Table 1. With the battery and all onboard sensors installed, the total takeoff weight of the aircraft is 1.72 kg, and its external dimensions with the arms extended are 0.560 m × 0.637 m. In this study, the direction corresponding to the 0.560 m dimension was defined as the forward direction of the aircraft for both the experiments and the numerical analysis. The propulsion system adopts a quadcopter configuration equipped with four 10.5-inch propellers. Flight data were acquired using the onboard measurement system. An exterior view of the aircraft is presented in Figure 1.

Table 1. SOTEN specifications

Total aircraft weight	1.72 kg
Aircraft sizes(x,y,z)	0.560 m , 0.153 m , 0.637 m
Propeller size	10.5 inches (0.2667 m)
Number of propeller blades	2
Number of propellers	4

ICCS Camera Ready Version 2026
To cite this paper please use the final published version:
DOI: 10.1007/978-3-032-29924-6_2

Fig. 1. Appearance of SOTEN

2.2 Definition of Coordinate Systems and Aircraft Configuration

Figure 2 illustrates the coordinate system and aircraft configuration definitions consistently used throughout the experiments and numerical analyses in this study. A right-handed coordinate system is adopted, with the aircraft center of gravity as the origin, the forward direction as the x-axis, the vertically upward direction as the y-axis, and the right-wing direction as the z-axis. The definitions of positive and negative rotation angles about each axis are as follows:

・Roll angle: Rotation about the x-axis. When viewed from the rear of the aircraft, a downward deflection of the right wing is defined as positive, and that of the left wing as negative.

・Pitch angle: Rotation about the z-axis. The horizontal attitude is defined as 0°, with nose-up rotation taken as positive and nose-down rotation as negative.

・Yaw angle: Rotation about the y-axis. When viewed from above, clockwise rotation is defined as positive and counterclockwise rotation as negative.

In addition, the arrangement and rotational directions of the four propellers are defined. The propellers located at the front right and rear left positions (Rotors 1 and 3) rotate counterclockwise (CCW) when viewed from above, whereas those at the front left and rear right positions (Rotors 2 and 4) rotate clockwise (CW).

ICCS Camera Ready Version 2026
To cite this paper please use the final published version:
DOI: 10.1007/978-3-032-29924-6_2

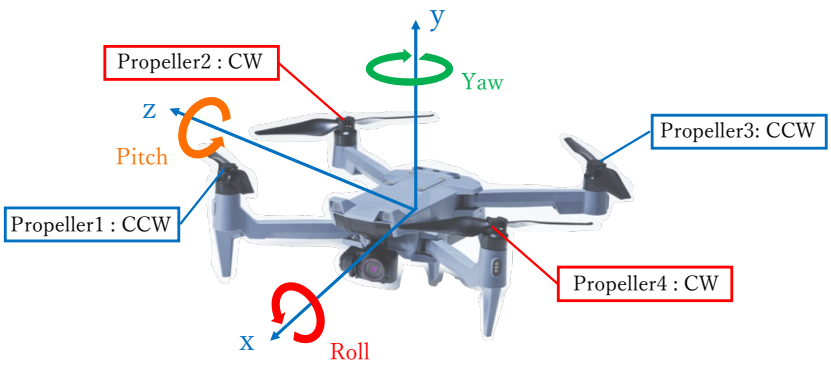

Fig. 2. Coordinate system and aircraft and propeller rotation directions

2.3 Wind Tunnel Facility

This experiment was conducted using the wind tunnel facility at the Fukushima Robot Test Field (RTF) [18]. The wind tunnel has a square test section with a cross-sectional area of 3.0 m × 3.0 m, providing sufficient spatial clearance for the test aircraft. Figure 3 shows the exterior view of the wind tunnel facility.

Fig. 3. Appearance of the wind tunnel

2.4 Experimental Conditions

The configuration of the wind tunnel test in this study is shown in Figure 4. The test aircraft was positioned 3500 mm downstream of the wind tunnel outlet and maintained in hover at the mid-height of the outlet cross-section. During the flight tests, the aircraft was controlled to maintain a fixed hovering position regardless of wind speed variations by combining the onboard self-positioning control system with visual corrections provided by the operator. Figure 5 shows the actual flight test setup.

In the experiment, the wind speed was incrementally increased from zero (0 m/s) to 5 m/s in 1 m/s increments. At each wind speed condition, after confirming that the aircraft

ICCS Camera Ready Version 2026
To cite this paper please use the final published version:
DOI: 10.1007/978-3-032-29924-6_2

had reached a sufficiently stable flight state, data were recorded for 10 seconds. The experimental values used for comparison with the numerical analysis are the time-averaged values obtained during this 10-second measurement period. The data sampling rate was 50 Hz.

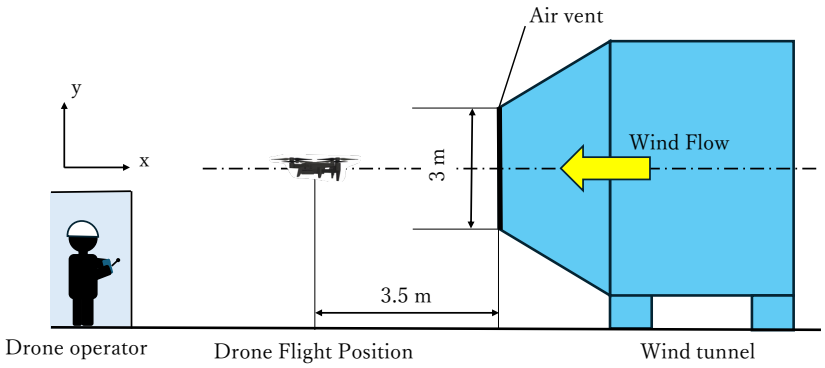

Fig. 4. Wind tunnel test configuration

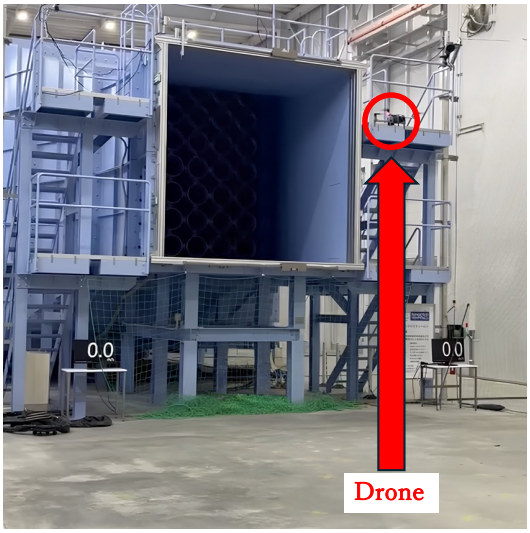

Fig. 5. Flight test overview

3 Numerical Approach

3.1 Fundamental Equation of Fluid Dynamics

In this study, the three-dimensional Euler equations, which govern inviscid compressible flow, are adopted to solve the flow field around the drone model with an emphasis

ICCS Camera Ready Version 2026
To cite this paper please use the final published version:
DOI: 10.1007/978-3-032-29924-6_2

on computational efficiency. The nondimensionalized form of the three-dimensional Euler equations is given as follows.

$$\frac{\partial \boldsymbol{q}}{\partial t}+\frac{\partial \boldsymbol{E}}{\partial x}+\frac{\partial \boldsymbol{F}}{\partial y}+\frac{\partial \boldsymbol{G}}{\partial z}=0, \tag{1}$$

$$\boldsymbol{q}=\begin{pmatrix}\rho\\ \rho u\\ \rho v\\ \rho w\\ e\end{pmatrix}, \boldsymbol{E}=\begin{pmatrix}\rho u\\ \rho u^2+p\\ \rho uv\\ \rho uw\\ u(e+p)\end{pmatrix}, \boldsymbol{F}=\begin{pmatrix}\rho v\\ \rho uv\\ \rho v^2+p\\ \rho vw\\ v(e+p)\end{pmatrix}, \boldsymbol{G}=\begin{pmatrix}\rho w\\ \rho uw\\ \rho vw\\ \rho w^2+p\\ w(e+p)\end{pmatrix} \tag{2}$$

Here,$\boldsymbol{q}$ denotes the vector of conserved variables; $\boldsymbol{E}$, $\boldsymbol{F}$, and $\boldsymbol{G}$ represent the inviscid flux vectors in the x-, y-, and z-directions, respectively; ρ is the fluid density; u, v, and w are the velocity components in the x-, y-, and z-directions; and e is the total energy per unit volume. The pressure p in Equation (2) is the gas pressure, which is determined from the ideal gas equation of state given in Equation (3), assuming an ideal gas.

$$p=(\gamma-1)\left[e-\frac{1}{2}\rho(u^2+v^2+w^2)\right] \tag{3}$$

Here, γ is the specific heat ratio, and in this study, γ was set to 1.4, the standard value for air at room temperature. For temporal discretization, a second-order Crank-Nicolson scheme was applied. For time integration, a pseudo-time inner iteration method based on an explicit two-stage rational Runge-Kutta scheme [19] was adopted, considering computational cost and stability. For spatial accuracy, a second-order extrapolation method was employed, combining gradient evaluation based on the Green-Gauss theorem with a vanLeer-like limiter function [20].

3.2 Fundamental Equation of Rigid Body

To describe the translational and rotational motion of the drone in three-dimensional space, the three-dimensional Newton–Euler equations are adopted as the governing equations for rigid-body dynamics. The three-dimensional Newton–Euler equations are expressed as follows.

$$m\ddot{\boldsymbol{r}}=\boldsymbol{f} \tag{4}$$

$$\boldsymbol{I}\dot{\boldsymbol{\omega}}+\boldsymbol{\omega}\times\boldsymbol{I}\boldsymbol{\omega}=\boldsymbol{\tau} \tag{5}$$

Here, m is the mass of the rigid body; $\boldsymbol{r}$ and $\boldsymbol{f}$ denote the position vector and the external force vector in three-dimensional space, respectively. $\boldsymbol{I}$ is the moment of inertia tensor, and $\boldsymbol{\omega}$ and $\boldsymbol{\tau}$ represent the angular velocity vector and the torque vector, respectively. Based on the above relationships, the six degrees of freedom associated with the rigid body's translational and rotational motions are described.

ICCS Camera Ready Version 2026
To cite this paper please use the final published version:
DOI: 10.1007/978-3-032-29924-6_2

3.3 Moving Computational Domain Method

This study employs the Moving Computational Domain (MCD) method [13], in which the computational domain moves in accordance with the motion of the object. Figure 6 presents a conceptual illustration of the MCD method. This approach is based on an unstructured moving-mesh finite volume method, enabling the simulation of free motion without constraints imposed by the computational domain while strictly satisfying the geometric conservation law. Furthermore, to reproduce the relative motion of multiple rotating axes, such as the four independently rotating propellers considered in this study, the MCD method is combined with a multi-axis sliding mesh method [15].

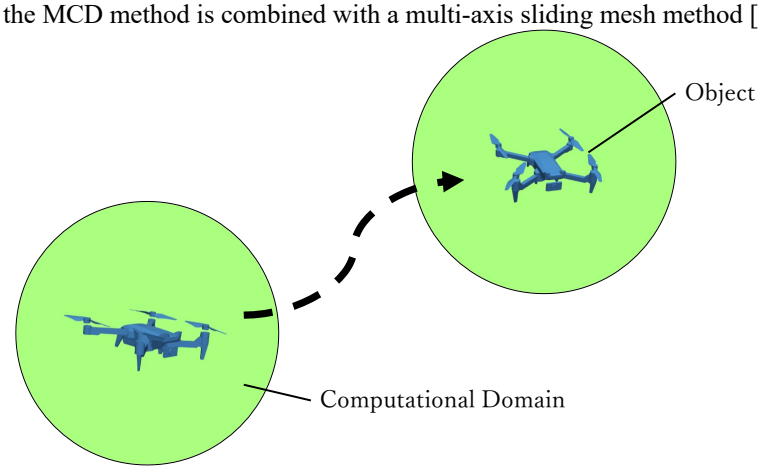

Fig. 6. Moving Computational Domain Method

4 Simulation Overview

4.1 Computational Grid

Figure 7 illustrates the computational domain and mesh configuration around the aircraft used in this study. The computational domain was defined as a spherical region with a radius approximately 15 times the aircraft length to adequately account for the propeller-induced downwash and its interaction with the surrounding flow field. As shown in Figure 7, a hierarchical mesh structure was adopted, with the grid progressively refined toward the vicinity of the aircraft. This approach captures the steep flow gradients around the object while optimizing computational cost. Figure 8 presents the surface mesh of the analyzed quadcopter drone. The aircraft model was developed based on the specifications of ACSL's small aerial photography drone, "SOTEN" [17]. Figure 9 shows the computational grids and their dimensions for each rotor region corresponding to the four propellers. The representative length used in this study is defined as the maximum aircraft width, including the distance between the propeller tips. The computational model was generated using the unstructured mesh generation software MEGG3D [21,22], resulting in a total of 1,269,880 cells in the entire domain. Each of

ICCS Camera Ready Version 2026
To cite this paper please use the final published version:
DOI: 10.1007/978-3-032-29924-6_2

the four independent rotor regions consists of 166,400 cells and has a diameter of 0.28 m. The minimum cell size on the rotor surface is approximately 1.5 mm.

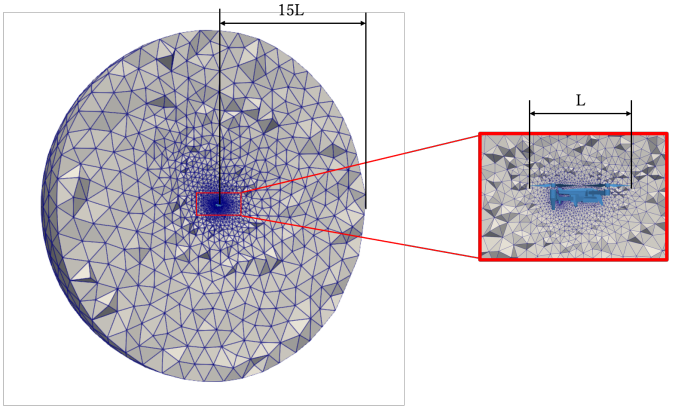

Fig. 7. Computational domain and grid configuration around the aircraft

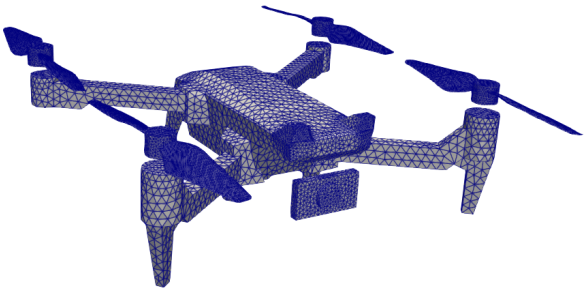

Fig. 8. Surface mesh of the quadcopter drone

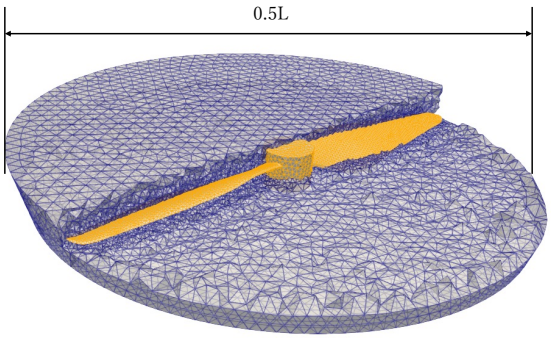

Fig. 9. Computational mesh of the propeller region and its size

ICCS Camera Ready Version 2026
To cite this paper please use the final published version:
DOI: 10.1007/978-3-032-29924-6_2

4.2 Computational Conditions

Table 2 summarizes the initial and boundary conditions used in the analysis. To replicate the headwind conditions anticipated during actual flight, the velocity components v and w were set to 0 m/s. For the streamwise component u, six inflow velocity cases were defined, ranging from 0 m/s to −5 m/s in increments of 1 m/s. Three types of boundary conditions were applied: slip wall conditions, Riemann invariant boundary conditions, and sliding mesh interfaces. Furthermore, in this analysis, all variables were nondimensionalized using representative values. The representative length was defined as the total aircraft length, $L = 0.56$ m; the representative density was set to the air density, $\rho = 1.247$ kg/m³; and the representative velocity was taken as the speed of sound, $V = 340.29$ m/s. The dimensionless time step was set to $dt = 2.0 \times 10^{-3}$.

Table 2. Initial and Boundary conditions

u	-5 ~ 0 m/s
v	0 m/s
w	0 m/s
Drone body surface	Slip wall condition
Outer boundary	Riemann invariant boundary condition
Propeller domain	Sliding mesh interface

4.3 Flight Simulation Conditions

In this study, simulations were conducted under six wind speed conditions ranging from 0 m/s to −5 m/s in 1 m/s increments, corresponding to the wind tunnel experiments. As the initial condition, either a quiescent state or a uniform flow in the negative x-direction was imposed throughout the computational domain, from which the aircraft motion was initiated. The following control conditions were applied to maintain the aircraft's position and attitude. Along the y-axis, the rotor rotational speed was adjusted so that the rotor thrust balanced gravity, thereby maintaining the target altitude. Along the x- and z-axes, the target ground speed of the aircraft was set to 0 m/s relative to the headwind entering from the +x direction. Under these conditions, the attitude angles required to sustain hovering were computed. This procedure reproduces the flight behavior in which the aircraft autonomously adjusts its attitude to counter external wind disturbances while attempting to maintain a fixed position. The computational results were time-averaged over approximately 1 second of physical time after the aircraft motion reached a dynamic equilibrium state and then compared with the experimental data.

5 Comparison of Experimental and Numerical Results

5.1 Qualitative Evaluation of the Flow Field

To qualitatively evaluate the flow field obtained from the numerical analysis, the velocity vectors around the aircraft and the pressure distribution on the aircraft surface are presented in Figure 10. Figure 10(a) shows the results under no-wind conditions (0

ICCS Camera Ready Version 2026
To cite this paper please use the final published version:
DOI: 10.1007/978-3-032-29924-6_2

m/s), whereas Figure 10(b) shows the results under headwind conditions (5 m/s). Compared with the no-wind condition in Figure 10(a), the velocity vectors in Figure 10(b) clearly indicate a uniform inflow from the front of the aircraft. This inflow accelerates downstream as it passes through the propellers, forming a downwash that extends beneath the aircraft. Furthermore, examination of the surface pressure distribution confirms that the pressure is lower on the upper surface and higher on the lower surface of each propeller. These results indicate that the fundamental aerodynamic characteristics of rotating wings are appropriately reproduced in the present analysis.

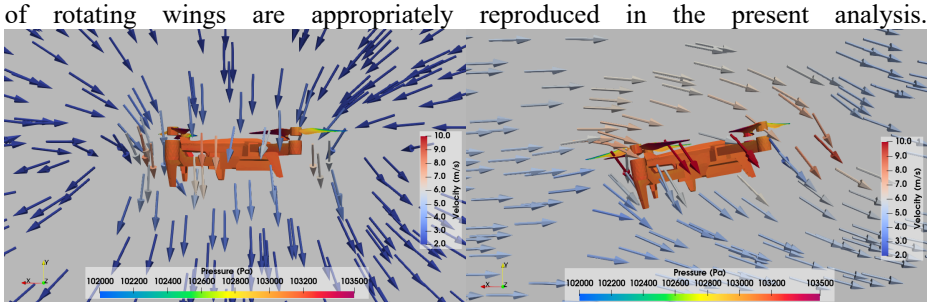

(a) No wind condition (0 m/s) (b) Headwind condition (5 m/s)

Fig. 10. Velocity vectors around the aircraft and surface pressure distribution

5.2 Comparison of Attitude Angles

Figure 11 shows the variation in the aircraft's attitude angles with wind speed. The horizontal axis represents the headwind speed, and the vertical axis represents the attitude angle. As shown in Figure 11, both the experimental and numerical results indicate that the pitch angle increases in the negative direction as the wind speed increases. This increase in forward tilt reflects the aircraft's response to maintain stationary hovering. To counteract the rearward aerodynamic drag induced by the headwind, a thrust component in the upwind direction is required. The quadcopter generates a horizontal propulsive component by tilting the aircraft forward, thereby redirecting part of the rotor thrust. Consequently, a larger forward tilt angle becomes necessary as the wind speed increases.

A detailed comparison of the pitch angle shows that the experimental values changed almost linearly from 0° under calm conditions to −8.29° at a wind speed of 5 m/s. Similarly, the numerical results varied from 0.17° under no-wind conditions to −9.85° at 5 m/s, generally reproducing the behavior of the actual aircraft. The absolute error in pitch angle at the maximum wind speed of 5 m/s was within 1.56°, demonstrating that this method provides sufficient accuracy for predicting the aircraft system's response to disturbance winds.

In contrast, discrepancies between the experimental and numerical results were observed for the roll and yaw angles. The roll angle remained close to 0° across all wind speeds, showing good agreement between experiment and analysis. The yaw angle, however, exhibited noticeable fluctuations in the experimental data. Under ideal conditions with a perfectly symmetrical airframe model and uniform inflow, the numerical

ICCS Camera Ready Version 2026
To cite this paper please use the final published version:
DOI: 10.1007/978-3-032-29924-6_2

analysis should theoretically yield zero yaw and roll angles in a headwind. The observed yaw deviations in the experiment are likely attributable to asymmetries in the experimental environment, such as minor structural distortions of the aircraft frame and slight nonuniformities in the wind speed distribution within the wind tunnel test section. These yaw deviations may cause the flight control system to adjust individual propeller rotational speeds to maintain attitude. Consequently, this effect may have contributed to the discrepancies between analytical and experimental results observed in the comparison of rotor rotational speeds discussed in Section 5.3, potentially influencing the accuracy of the pitch angle prediction. Future work should focus on identifying subtle disturbance factors in the experimental environment and refining the analytical model to account for these effects.

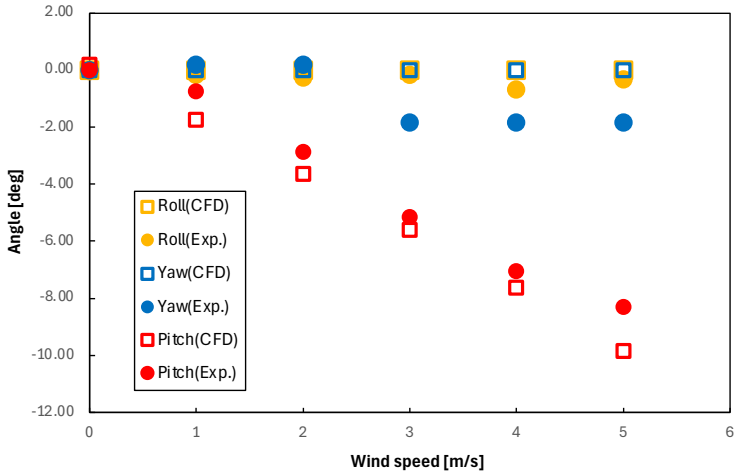

Fig. 11. Comparison of attitude angles with respect to wind speed

5.3 Comparison of Rotor Rotation Speeds

Figure 12 illustrates the variation in the rotational speed of each rotor with wind speed. The horizontal axis represents the wind speed, and the vertical axis represents the rotational speed. Here, P1 and P4 correspond to the front rotors, whereas P2 and P3 correspond to the rear rotors. The figure indicates that, in both the experimental and numerical results, the rotational speeds of the front rotors decrease as the wind speed increases, while those of the rear rotors increase or remain at relatively high levels. This trend supports the generation of a pitch-down moment that raises the rear of the aircraft, thereby forming the forward-leaning attitude described in Section 5.2.

A comparison between the experimental and numerical results shows that the numerical values are consistently higher than the experimental values over the entire wind speed range. To quantitatively assess this difference, the relative error ε was calculated using the following equation, taking the experimental values as the reference.

ICCS Camera Ready Version 2026
To cite this paper please use the final published version:
DOI: 10.1007/978-3-032-29924-6_2

$$\varepsilon = \frac{N_C - N_E}{N_E} \tag{6}$$

Here, N_C represents the rotor rotational speed obtained from the numerical analysis, whereas N_E denotes the rotor rotational speed measured in the wind tunnel experiments. Table 3 summarizes the range of relative errors for all rotors at each wind speed. The relative error ranged from 7.6 % to 11.1 % under no-wind conditions and from 4.1 % to 14.9 % at the maximum wind speed. One possible contributing factor is the underestimation of thrust in the numerical analysis. As a result, the thrust generated at a given rotational speed was predicted to be smaller than that of the actual aircraft. It is therefore inferred that, in the analysis, the control system set higher rotational speeds than those of the actual aircraft in order to maintain position while supporting the aircraft weight.

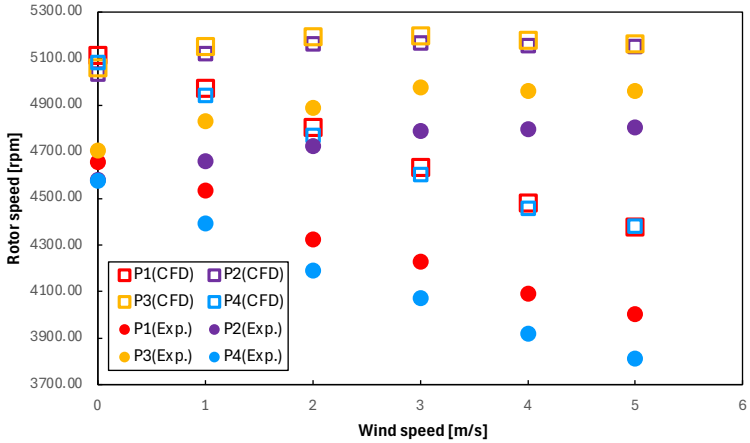

Fig. 12. Comparison of individual rotor speeds with respect to wind speed

Table 3. Relative error of rotor speed at each wind speed

Wind speed [m/s]	Propeller1 [%]	Propeller2 [%]	Propeller3 [%]	Propeller4 [%]
0	9.8	9.9	7.6	11.1
1	9.7	9.9	6.7	12.5
2	11.1	9.3	6.2	13.8
3	9.5	7.9	4.4	13.0
4	9.5	7.5	4.4	13.7
5	9.4	7.2	4.1	14.9

6 Conclusions

This study verified the validity of a coupled fluid–rigid body motion analysis combining the MCD method with a multi-axis sliding mesh method. By comparing numerical

ICCS Camera Ready Version 2026
To cite this paper please use the final published version:
DOI: 10.1007/978-3-032-29924-6_2

results obtained from an inviscid fluid model with wind tunnel experimental data for quadcopter behavior under disturbance winds, the following findings were obtained.

First, with respect to attitude angle reproducibility, the proposed method was confirmed to accurately capture the aircraft's forward-tilting response to disturbance winds. Specifically, the pitch angle error remained within 1.56° at the maximum wind speed, demonstrating sufficient accuracy in predicting the aircraft's dynamic equilibrium state. However, slight deviations in the roll and yaw angles were found to cause discrepancies in propeller rotational speeds, potentially affecting the accuracy of the attitude angle prediction. Furthermore, the rotational speed profiles of each rotor indicated that the numerical results were approximately 10 % higher overall than the experimental values. This discrepancy is primarily attributed to the underestimation of thrust in the numerical analysis. Nevertheless, a very high correlation was observed between the experimental and numerical results in terms of the rotational speed trends with increasing wind speed. Based on these results, the present method employing an inviscid fluid model can be regarded as an effective approach for constructing a digital twin capable of rapidly predicting the dynamic response of an actual aircraft with practical accuracy.

To further improve the prediction accuracy of rotor rotational speeds, which remains a challenge identified in this study, it is necessary to introduce a model that accounts for mesh resolution on the propeller blade surfaces. In addition, more advanced modeling that incorporates detailed airframe geometry and potential asymmetries in the experimental environment is expected to enhance prediction accuracy under more complex and realistic flight conditions.

Acknowledgments. This paper is based on results obtained from a project, JPNP14004, subsidized by the New Energy and Industrial Technology Development Organization (NEDO).

References

1. Zhijun, M., Jiachi, J., Lulu, L., Siyuan, L., Zhen, S., Qingfang, X., Zikang, Y.: eVTOL aircraft for the low-altitude economy: A review of development history, core technologies, and future trends. Case Studies on Transport Policy **22**, 101629 (2025)
2. Ruiz, M.C., Scanavino, M., D'Ambrosio, D., Guglieri, G., Vilardi, A.: Experimental and numerical analysis of multicopter rotor aerodynamics. In: AIAA Aviation 2021 Forum. AIAA 2021-2539 (2021)
3. Gordillo, P., Andres, M., Santos, V., Sebastian, J., Mejia, L., Omar, D., Collazos, S., Juliana, L., Escobar., Jaime A.: Numerical and Experimental Estimation of the Efficiency of a Quadcopter Rotor Operating at Hover. Energies **12**(2), 261 (2019)
4. Tanabe, Y., Sugawara, H., Sunada, S., Yonezawa, K., Tokutake, H.: Quadrotor Drone Hovering in Ground Effect. Journal of Robotics and Mechatronics **33**(2), 339-347 (2021)
5. Herz, S., Atte, A., Seth, D., Rauleder, J., McCrink, M.: Effects of rotor-rotor and rotor-body interactions on quadrotor vehicle performance for multiple flight configurations. Aerospace Science and Technology **158**, 109873 (2025)
6. Kyoto Institute of Technology: Trademark "Digital Flying Car" (Registration No. 6705590), registered June 8 (2023)

ICCS Camera Ready Version 2026
To cite this paper please use the final published version:
DOI: 10.1007/978-3-032-29924-6_2

7. Gomi, R., Takii, A., Yamakawa, M., Asao, S., Takeuchi, S., Nishimura, M.: Flight simulation from takeoff to yawing of eVTOL airplane with coaxial propellers by fluid-rigid body interaction. Advances in Aerodynamics **5**(1), 2 (2023)
8. Takii, A., Gomi, R., Yamakawa, M., Tsubokura, M.: Turning flight simulation with fluid-rigid body interaction for flying car with contra-rotating propellers. In: ICCS 2023, pp. 566-577. (2023)
9. Takahashi, N., Gomi, R., Takii, A., Yamakawa, M., Asao, S., Takeuchi, S.: Numerical Simulation of the Octorotor Flying Car in Sudden Rotor Stop. In: ICCS 2023, pp. 33-46. (2023)
10. Magata, T., Takii, A., Yamakawa, M., Kobayashi, Y., Asao, S., Takeuchi, S.: Effects of wind on forward and turning flight of flying cars using computational fluid dynamics. In: ICCS 2024, pp. 3-18. (2024)
11. Azid, S.I., Kumar, K., Cirrincione, M., Fagiolini, A.: Wind gust estimation for precise quasi-hovering control of quadrotor aircraft. Control Engineering Practice **116**, 104930 (2021)
12. Ferreira, D., De Paula, A.A., Secco, N.R., Galdino da Silva, R.: Validation of inviscid CFD analysis for the Generic Future Fighter. In: 27th Brazilian Congress of Thermal Sciences and Engineering. COB2023-1927 (2023)
13. Yamakawa, M., Mitsunari, N., Asao, S.: Numerical simulation of rotation of intermeshing rotors using added and eliminated mesh method. Procedia Computer Science **108**, 1883-1892 (2017)
14. Yamakawa, M., Takekawa, D., Matsuno, K., Asao, S.: Numerical simulation for a flow around body ejection using an axisymmetric unstructured moving grid method.: Computational Thermal Sciences: An International Journal **4**(3), 217-223 (2012)
15. Takii, A., Yamakawa, M., Asao, S., Tajiri, K.: Six degrees of freedom flight simulation of tilt-rotor aircraft with nacelle conversion. Journal of Computational Science **44**, 101164 (2020)
16. Yamakawa, M., Kita, Y., Matsuno, K.: Domain decomposition method for unstructured meshes in an OpenMP computing environment. Computers & Fluids **45**(1), 168-171 (2011)
17. ACSL Inc Homepage. https://www.acsl.co.jp/. last accessed 2026/01/20
18. Fukushima Robot Test Field Homepage, https://rtf.f-rei.go.jp/, last accessed 2026/01/20
19. Wambecq, A.: Rational Runge-Kutta methods for solving systems of ordinary differential equations. Computing **20**(4), 333-342 (1978)
20. Hishida, M., Hashimoto, A., Murakami, K., Aoyama, T.: A new slope limiter for fast unstructured CFD solver FaSTAR. In: Proceedings of the 42nd Fluid Dynamics Conference / Aerospace Numerical Simulation Symposium 2010, JAXA Special Publication, JAXA-SP-10-012. Japan Aerospace Exploration Agency (JAXA) (2011)
21. Ito, Y., Nakahashi, K.: Surface triangulation for polygonal models based on CAD data. International Journal for Numerical Methods in Fluids **39**(1), 75-96 (2002)
22. Ito, Y.: Challenges in unstructured mesh generation for practical and efficient computational fluid dynamics simulations. Computers & Fluids **85**(1), 47-52 (2013)

ICCS Camera Ready Version 2026
To cite this paper please use the final published version:
DOI: 10.1007/978-3-032-29924-6_2